第 48 卷 第 13 期/2021 年 7 月/中国激光 研究论文

中国激光

1064 nm 侧向微结构宽脊波导半导体激光器

齐军，邹永刚*，范杰**，杨晶晶，刘莹，马晓辉

长春理工大学高功率半导体激光国家重点实验室，吉林 长春 130022

摘要 1064 nm 半导体激光器在光纤通信系统方面有重大应用，但随着脊波导宽度增加，出现输出模式增加，近场光斑“多瓣”现象，导致其光束质量降低，影响其光纤耦合效率。为此提出一种侧向微结构宽脊波导半导体激光器，根据其腔内各阶侧模光场分布特点，在宽脊两侧引入微结构，以此增大高阶侧模衍射损耗，提高高阶侧模阈值增益，增大基侧模与高阶侧模的阈值增益差，消除近场光斑“多瓣”现象，改善侧向光束质量。在条宽 120 μm、腔长 1 mm 的结构参数下，制作了宽脊波导半导体激光器和具有侧向微结构的激光器件。测试结果表明，在输入电流为 0.5 A 时，与宽脊波导半导体激光器相比，引入侧向微结构后器件输出功率提升了 58.5%，斜率效率提升了 80%，电光转换效率提升了 55.9%。

关键词 激光器；半导体激光器；侧向微结构；侧向模式；阈值增益；近场光斑

中图分类号 TN365 **文献标志码** A **doi**：10.3788/CJL202148.1301003

1 引 言

半导体激光器具有效率高[1]、易集成[2]、可靠性高[3]、易调谐[4-5]等优点，使其具有广泛应用前景，如光纤耦合[6]、光纤激光器的种子源、医疗设备[7]、通信系统[8-10]等。为了提高半导体激光器的输出功率，通常采用宽脊波导结构[11-12]，但其输出模式差，能量分布不均匀，主要体现在近场光斑“多瓣”现象，限制其在应用上的广泛性。

为改善半导体激光器的侧向模式差这一现象，研究学者们提出了许多解决措施。1989 年 Sharfin 等[13]提出的外腔激光器结构，包括棱镜和传统的外腔镜面，高阶模式的过滤是通过激光器本身来实现的，这种结构使得外腔设计更加精简，但工艺复杂且基模输出功率仅为 100 mW；1992 年由 Walpole 等[14-15]提出锥形波导半导体激光器，以窄条对高阶侧模进行过滤实现高光束质量为目的，锥形部分主要是对功率进行放大作用，这种结构可实现高功率和高光束质量结合[16]，但其具有较高的像散[17]，需要额外的光学元件进行光束校正；2004 年，美国伊利诺伊大学 Swint 等[18]提出通过利用弯曲波导来增加高阶模在波导中传输的损耗，进而达到对高阶侧向模式的抑制效果，但其比同宽度直波导半导体激光器的阈值电流提高了 5%～10%。虽然以上方法均可改善侧向模式，提高侧向光束质量，但都或多或少存在一定的缺点。

本文提出了一种侧向微结构半导体激光器(LMWR-LD)，基于宽脊波导半导体激光器(WR-LD)腔内各阶侧模光场分布特点，通过在宽脊波导两侧刻蚀微结构增加高阶侧模的散射损耗，以此增加基侧模与高阶侧模的阈值增益差，从而抑制激光器高阶侧模输出，消除侧向光斑“多瓣”现象，改善侧向光束质量，在减小腔内模式竞争的同时提升激光器的输出功率、斜率效率及电光转换效率。

2 器件制备及原理分析

LMWR-LD 器件结构如图 1(a)所示，在宽脊波导两侧刻蚀三角形区域，形成梯形结构侧壁。采用金属有机化学气相沉积法(MOCVD)在 350 μm 厚的 GaAs 衬底片上生长外延结构，有源区为厚度是

收稿日期：2020-11-05；**修回日期**：2020-12-06；**录用日期**：2021-01-11

基金项目：吉林省科技发展计划项目(20190302052GX，20200519018JH)、吉林省教育厅“十三五”科学技术项目(JJKH20190543KJ)

通信作者：*zouyg@cust.edu.cn；**fanjie@cust.edu.cn

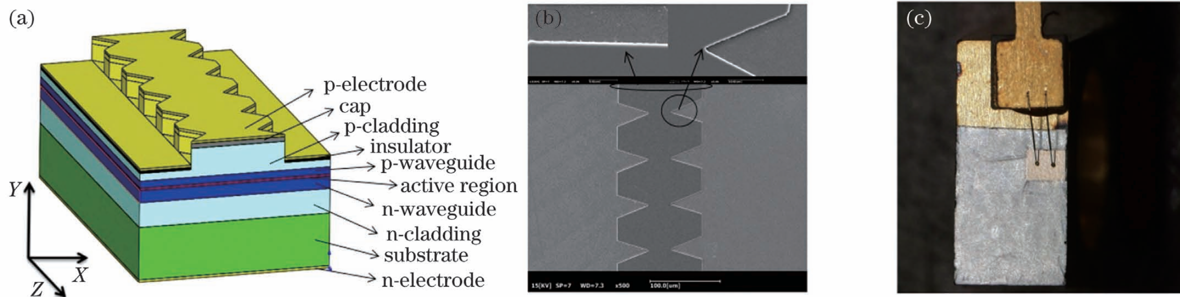

图 1 侧向微结构宽脊波导半导体激光器。(a)器件结构图;(b)侧向微结构宽脊波导 SEM 图;(c)封装后的管芯图

Fig. 1 Lateral microstructure wide-ridge waveguide semiconductor laser. (a) Device structure diagram; (b) SEM image of lateral microstructure wide-ridge waveguide; (c) packaged device diagram

6 nm/6 nm/1.7 nm 的 $In_{0.34}Ga_{0.66}As$ / $Ga_{0.17}As_{0.83}P$ /GaAs 材料,N 型和 P 型限制层均为厚度是 1 μm 的 $Al_{0.5}Ga_{0.5}As$,N 型和 P 型波导层分别为厚度是 150 nm 的 $Al_{0.3}Ga_{0.7}As$ 和 450 nm 的 $Al_{0.3}Ga_{0.7}As$ 材料,为了使器件具有良好的欧姆接触,在 P 面最上层生长了一层厚度为 200 nm 的高掺 GaAs 盖层,具体外延结构参数如表 1 所示。侧向微结构宽脊波导为一次光刻形成,采用电感耦合等离子体(ICP)干法刻蚀,通过优化气体流量以及刻蚀时间得到平整的腔面及侧向微结构侧壁,如图 1(b)扫描电镜图(SEM)所示,脊刻蚀深度为 680 nm,脊宽度为 120 μm,两侧微结构宽度均为 35 μm。采用等离子体增强化学气相沉积法(PECVD)沉积 300 nmSiO_2 绝缘层,防止电流从脊外注入,磁控溅射 P 面电极,减薄抛光至 120 μm 厚度,磁控溅射 N 面电极,合金退火。解理完成的管芯采用 C-Mount 封装,封装时管芯 P 面向下,通过贴绝缘子和焊金丝的方式,将管芯的 N 面电极引出并实现其与铜热沉的电隔离,封装后的管芯如图 1(c)所示。测试时,电源正极连接铜热沉,电源负极连接绝缘子。

表 1 外延层结构参数

Table 1 Structure parameters of epitaxial layer

Number	Type	Material	Thickness d /μm	Doping level /cm^{-3}	Average refractive index
1	Cap	GaAs	0.2000	2×10^{20}	3.48
2	p-cladding	$Al_{0.5}Ga_{0.5}As$	1.0000	1×10^{18}	3.23
3	p-waveguide	$Al_{0.3}Ga_{0.7}As$	0.1500		3.34
4		GaAs	0.0017		
5		$Ga_{0.17}As_{0.83}P$	0.0060		
6	Active region	$In_{0.34}Ga_{0.66}As$	0.0060		3.66
7		$Ga_{0.17}As_{0.83}P$	0.0060		
8		GaAs	0.0017		
9	n-waveguide	$Al_{0.3}Ga_{0.7}As$	0.4500		3.34
10	n-cladding	$Al_{0.5}Ga_{0.5}As$	1.0000	1×10^{18}	3.23

图 2 为 Pics3d 仿真软件模拟宽为 120 μm 的 WR-LD 输出模式特性,由于不同模式的光场分布不同,其能量分布也不同。基侧模光斑为单个光斑,分布呈高斯分布,能量主要集中在宽脊波导中心位置处;一阶侧模光斑中间有一条断线,光斑被一分为二,变为两个光斑,能量分布不均匀,主要分布在宽脊波导两侧;随着模式数目的不断增加,其对应光斑中的断线处越多,光斑数目越多,能量分布越不均匀,五阶侧模光斑中间出现五条断线,将光斑分成六瓣,能量分布也更加分散。由于 WR-LD 模式竞争激烈,输出模式数目多,所以其近场光斑呈现出“多瓣”现象。

为抑制高阶侧模输出,消除 WR-LD 近场光斑“多瓣”现象,从模式阈值增益角度分析,模式阈值增益公式为

$$g_{th}=\alpha_i+(1/L)\ln(1/R), \tag{1}$$

式中:g_{th} 为阈值增益;L 为腔长;R 为腔面反射率;α_i 为腔内损耗,在此只考虑衍射损耗。可知,在同

一器件条件下，为了增大高阶侧模的阈值增益，可增大高阶侧模的衍射损耗，因此在宽脊两侧引入微结构，如图 2 所示。侧向微结构的宽度在脊波导两侧逐渐增加，由Ⅰ到Ⅱ进入脊内，随着侧向微结构宽度的增加，其与各阶侧模的交叠区域增加，即衍射损耗区域增加，由于高阶侧模的能量主要分布在宽脊波导两侧，基侧模能量主要集中在宽脊波导中心，则随着侧向微结构宽度的增加，高阶侧模的衍射损耗大于基侧模的衍射损耗，高阶侧模的阈值增益大于基侧模的阈值增益。

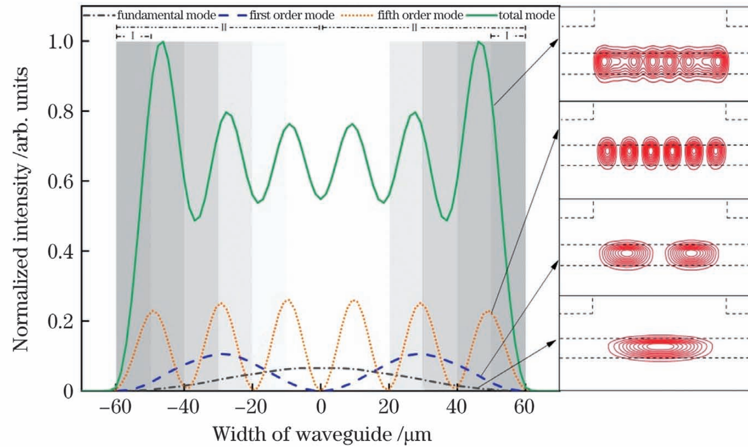

图 2 WR-LD 模式分布图

Fig. 2 Modes distribution diagram of WR-LD

基于 WR-LD 内各阶侧模光场分布特点，使用时域有限差分 FDTD 模拟软件分析侧向微结构对各阶侧向模式光场分布的作用机理。图中纵坐标表示脊波导宽度，横坐标表示腔长，光源中心波长为 1064 nm，由左往右入射经过侧向微结构宽脊波导，两侧为刻蚀结构。图3(a)～(c)为基侧模、一阶侧

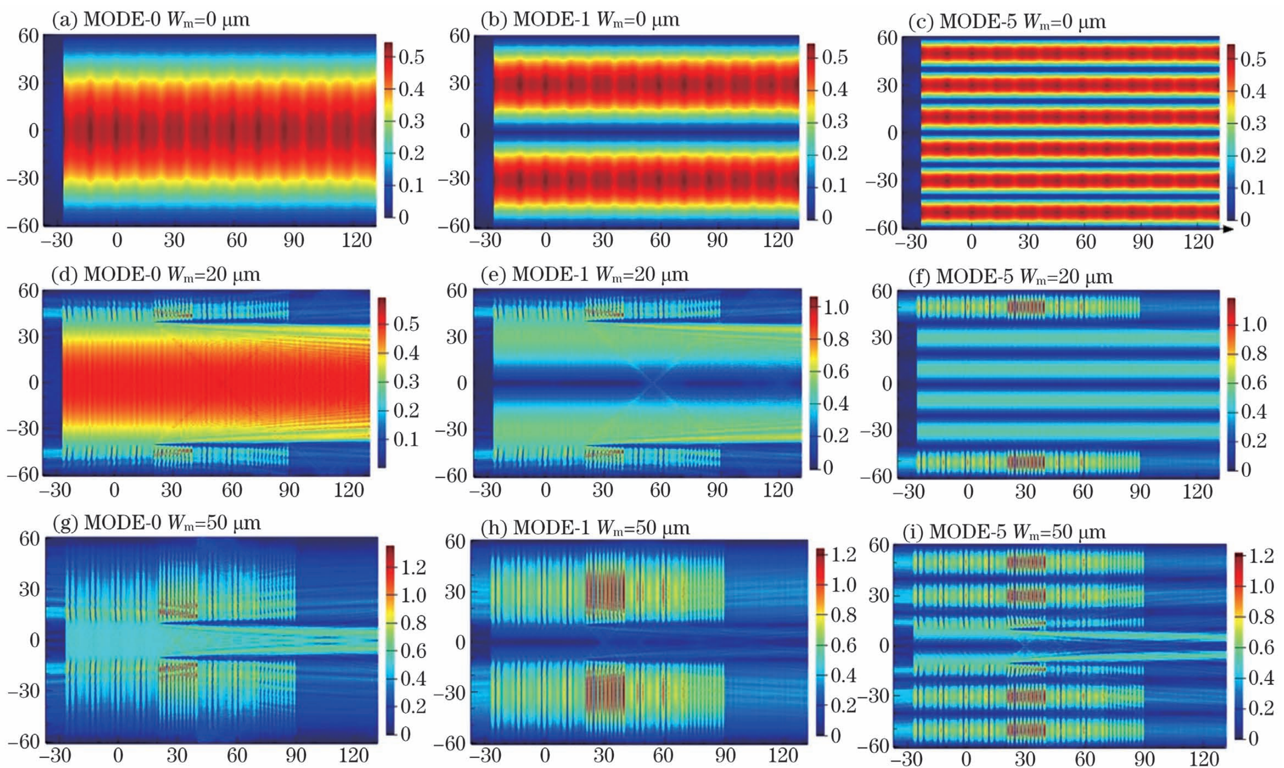

图 3 不同宽度的侧向微结构与各阶侧模光场分布关系图。(a)～(c)侧向微结构宽度为 0 μm；(d)～(f)侧向微结构宽度为 20 μm；(g)～(i)侧向微结构宽度为 50 μm

Fig. 3 Relationship between the lateral microstructures of different widths and the optical field distribution of each lateral mode. (a)-(c) Lateral microstructure width is 0 μm; (d)-(f) lateral microstructure width is 20 μm; (g)-(i) lateral microstructure width is 50 μm

模、五阶侧模三种模式的光场分布图，可以看出，基侧模能量主要集中分布在脊波导中心，一阶侧模能量主要分布在两侧，模式数目越高，能量越分散。针对高阶侧模的光场分布，在脊波导两侧刻蚀 20 μm 宽的侧向微结构，其光场分布如图 3(d)～(f)所示，相比基侧模，高阶侧模在侧向微结构作用区域明显存在局域场强，表明其损耗更高。随着侧向微结构宽度增加到 50 μm，如图 3(g)～(i)所示，光场与侧向微结构交叠的区域增大，各阶侧模的损耗均有所增加，但是由于各阶模式的光场分布不同，侧向微结构对其损耗大小有所差别。

进一步分析各阶侧模经过侧向微结构波导后的损耗。在此模拟中，材料吸收系数设为 0，各阶侧模的透过率为 T，反射率为 R，因此侧向微结构引起的衍射损耗表示为 $1-T-R$。图 4(a)给出了不同侧向微结构宽度与各阶侧模的损耗关系，随着侧向微结构宽度增加，各阶侧模衍射损耗均增大，但增大幅度有所不同，并非单调递增分布。图 4(b)表明了侧向微结构宽度对基侧模与高阶侧模的损耗差的影响，在侧向微结构宽度为 30 μm 时，一阶侧模损耗为 0.118，二阶侧模损耗为 0.336，此后高阶侧模损耗趋于平缓，损耗差为 0.218。随着侧向微结构宽度增加，各阶侧模损耗趋势相似，但损耗差有所不同，当侧向微结构宽度为 35 μm 时，基侧模与一阶侧模损耗差为 0.283；当微结构宽度进一步增加到 40 μm 时，基侧模与一阶侧模损耗差为 0.232，因此在侧向微结构宽度为 35 μm 时存在最大模式损耗差为 0.283。

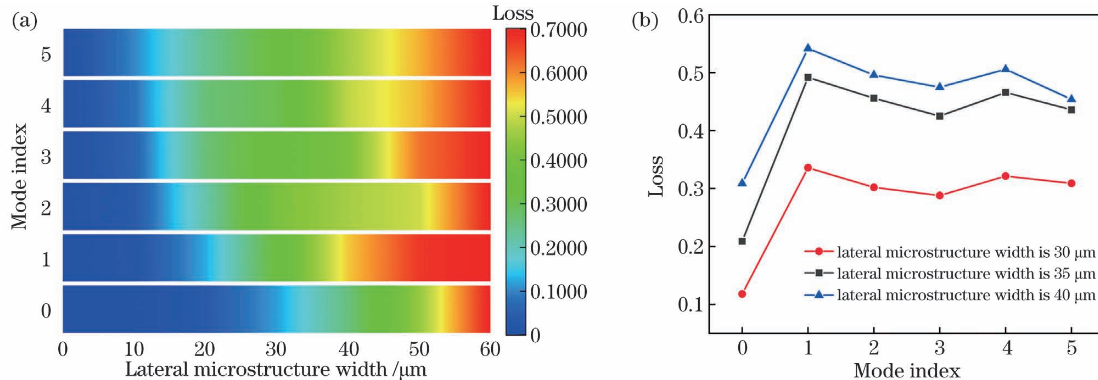

图 4　模式损耗图。(a)不同宽度的侧向微结构与各阶侧模损耗关系图；(b)不同宽度的侧向微结构与模式损耗差关系图

Fig. 4　Mode loss graphs. (a) Relationship between the lateral microstructures of different widths and the loss of each lateral mode; (b) relationship between the lateral microstructure of different widths and the mode loss difference

3　器件测试

将封装后的器件进行测试，测试所用的 CCD 物镜倍数为 4.5 倍，物镜最前方加置 2 倍放大物镜，使用透过率为 0.3% 的衰减片，在输入电流为 0.5 A 时测得近场光斑。图 5(a)为 WR-LD 近场光斑，可以明显看出光斑在侧向有许多断线处，呈现“多瓣”现象；图 5(b)为 LMWR-LD 近场光斑，发现其光斑在侧向上无断线处，呈现单个光斑现象，最大限度地消除了光斑侧向“多瓣”现象；图 5(c)显示了两种器件的近场分布，相较于 WR-LD 的近场分布，LMWR-LD 近场边缘处的强度减小，这是由于侧向微结构对高阶侧模起到了抑制作用，与前文分析相一致。因为 LMWR-LD 消除了近场光斑“多瓣”现象，所以其远场光斑呈现“单瓣”现象，其水平发散角由 2.07° 减小到 2.05°，并测得其中心波长为 1064.2 nm，如图 6 所示。

两种器件的(L-I-V)特性曲线如图 7(a)所示，WR-LD 阈值电流为 100 mA，随着输入电流的增加，输出功率呈上升趋势，在输入电流 $I=0.5$ A 时，电压为 1.75 V，输出功率为 82 mW，斜率效率为 0.15 W/A。在引入宽度为 35 μm 的侧向微结构后，LMWR-LD 电压为 1.8 V，输出功率为 130 mW，斜率效率为 0.27 W/A。与 WR-LD 相比 LMWR-LD 输出功率提升了 58.5%，斜率效率提升了 80%。由于 LMWR-LD 输出功率的提升，其电光转换效率也提升到 14.5%，与 WR-LD 的电光转换效率 9.3% 相比，电光转换效率提升了 55.9%，如图 7(b)所示。经分析认为 LMWR-LD 输出功率的提升存在两方面的原因，一方面是因为在 120 μm 宽脊上引入微结构后，在同一输入电流的情况下电流注入区面积减小，导致电流密度增加，以至其输出功率提高，经过计算发现在同一电流密度下，引入微结构后的LMWR-LD输出功率仍大于WR-LD的输出功

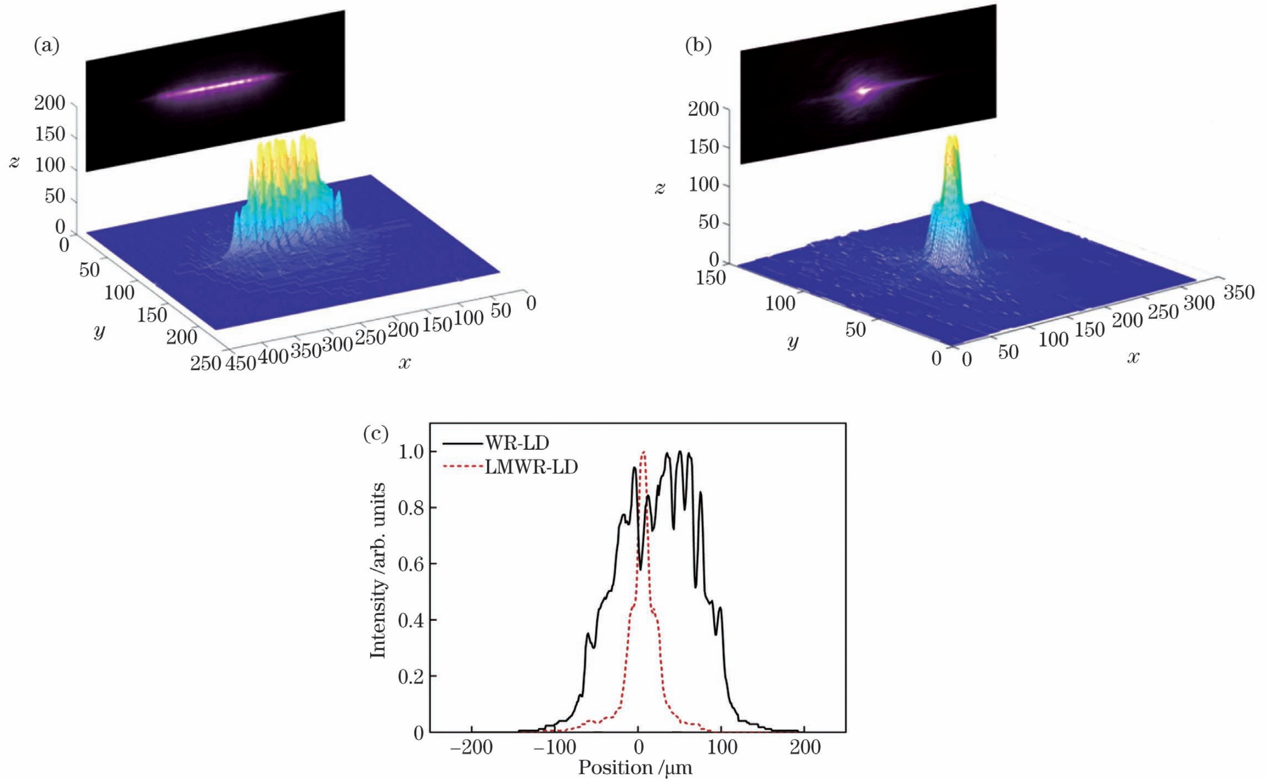

图 5　近场光斑分布图。(a)WR-LD 三维近场光斑图;(b)LMWR-LD 三维近场光斑图;(c)二维近场分布图

Fig. 5　Near-field spot patterns. (a) WR-LD three-dimensional near-field spot pattern; (b) LMWR-LD three-dimensional near-field spot pattern; (c) two-dimensional near-field distribution pattern

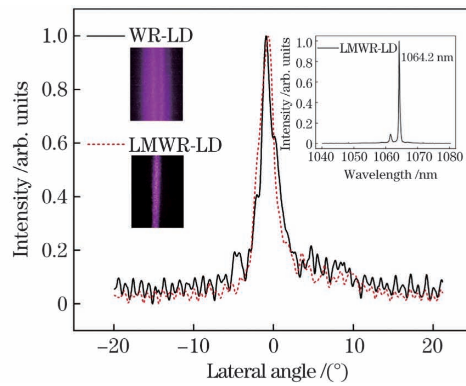

图 6　侧向发散角图

Fig. 6　Schematic diagram of lateral divergence angle

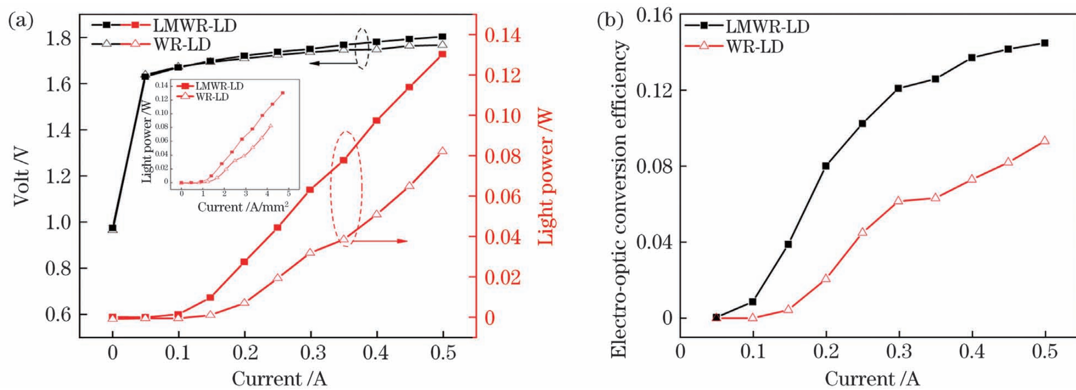

图 7　器件特性曲线图。(a)L-I-V 特性曲线图;(b)电光转换效率特性曲线图

Fig. 7　Device characteristic curves. (a) L-I-V characteristic curves; (b) electro-optic conversion efficiency characteristic curves

率,但输出功率差减小,如图 7(a)中插图所示;另一方面则是因为在引入侧向微结构后宽脊波导半导体激光器腔内高阶侧模被抑制[19-20],降低了腔内模式竞争,使输出光斑更加均匀,呈高斯分布,与注入电流的匹配度更高[19]。

4 结 论

本文提出了一种侧向微结构宽脊波导半导体激光器,通过在宽脊两侧引入微结构增大高阶侧模的衍射损耗,从而增加了基侧模与高阶侧模的阈值差,实现了高阶侧模抑制,最大限度地消除了光斑“多瓣”现象。该激光器件的侧向微结构与宽脊波导为同一次紫外光刻形成,具有工艺简单、成本低的优点。同时,制备了侧向微结构宽脊波导半导体激光器器件,并对其封装后的器件测试,与宽波导半导体激光器相比,在输入电流为 0.5 A 时,器件输出功率由 82 mW 提升到 130 mW,斜率效率由 0.15 W/A 提高到 0.27 W/A,电光转换效率由 9.3%提高到 14.5%,近场光斑侧向“多瓣”现象得到最大化消除。但器件性能还有待提升,后续可以在外延生长及工艺方面进一步优化,得到更好的器件测试结果。

参 考 文 献

[1] Xiong C, Chong F, Wang J, et al. Doping profile optimization and design of waveguide layer for laser diode with high conversion efficiency [J]. Semiconductor Optoelectronics, 2010, 31(1): 16-19, 54.
熊聪, 崇锋, 王俊, 等. 高效率半导体激光器波导层掺杂的优化设计[J]. 半导体光电, 2010, 31(1): 16-19, 54.

[2] Wang H, Zhang R K, Lu D, et al. 1.55 μm high-power high-speed directly modulated semiconductor laser array[J]. Acta Optica Sinica, 2019, 39(9): 0914001.
王皓, 张瑞康, 陆丹, 等. 1.55 μm 大功率高速直调半导体激光器阵列[J]. 光学学报, 2019, 39(9): 0914001.

[3] Yuan Q H, Jing H Q, Zhong L, et al. High-power and high-reliability 9XX-nm laser diode[J]. Chinese Journal of Lasers, 2020, 47(4): 0401006.
袁庆贺, 井红旗, 仲莉, 等. 高功率高可靠性 9XX nm 激光二极管[J]. 中国激光, 2020, 47(4): 0401006.

[4] Zorabedian P, Trutna W, Cutler L. Bistability in grating-tuned external-cavity semiconductor lasers [J]. IEEE Journal of Quantum Electronics, 1987, 23(11): 1855-1860.

[5] Zheng Z, Zou Y G, Shi L L, et al. High-contrast grating structure design for liquid crystal tunable vertical-cavity surface-emitting lasers[J]. Laser & Optoelectronics Progress, 2020, 57(1): 011402.
郑舟, 邹永刚, 石琳琳, 等. 液晶可调谐 VCSEL 中高对比光栅结构的设计[J]. 激光与光电子学进展, 2020, 57(1): 011402.

[6] Yu H, Ma X H, Zhao X, et al. Fiber coupling technology based on diode laser stack[J]. Chinese Journal of Lasers, 2017, 44(11): 1101006.
于贺, 马晓辉, 赵鑫, 等. 基于半导体激光器堆栈的光纤耦合技术[J]. 中国激光, 2017, 44(11): 1101006.

[7] Gaimard Q, Triki M, Nguyen-Ba T, et al. Distributed feedback GaSb based laser diodes with buried grating: a new field of single-frequency sources from 2 to 3 μm for gas sensing applications [J]. Optics Express, 2015, 23(15): 19118-19128.

[8] Lu D, Yang Q L, Wang H, et al. Review of semiconductor distributed feedback lasers in the optical communication band[J]. Chinese Journal of Lasers, 2020, 47(7): 0701001.
陆丹, 杨秋露, 王皓, 等. 通信波段半导体分布反馈激光器[J]. 中国激光, 2020, 47(7): 0701001.

[9] Zhou Q, Liu J L, Gu Y H, et al. Gain-switched semiconductor pulsed laser for quantum secure communication[J]. Chinese Journal of Lasers, 2016, 43(5): 0502005.
周强, 刘金璐, 谷远辉, 等. 量子保密通信用增益开关半导体脉冲激光器[J]. 中国激光, 2016, 43(5): 0502005.

[10] Pan X M, Wu Z M, Tang X, et al. Chaos synchronization and communication in mesh network based on mutually coupled semiconductor lasers[J]. Chinese Journal of Lasers, 2013, 40(12): 1202005.
潘兴茂, 吴正茂, 唐曦, 等. 基于互耦半导体激光器的混沌网状网络的同步与通信[J]. 中国激光, 2013, 40(12): 1202005.

[11] Tan S Y, Wang H, Zhang R K, et al. High power high beam quality 1060 nm large optical cavity asymmetric waveguide semiconductor laser diode[J]. Acta Optica Sinica, 2015, 35(s1): s114006.
谭少阳, 王皓, 张瑞康, 等. 大功率高光束质量 1060 nm 大光腔非对称波导半导体激光二极管[J]. 光学学报, 2015, 35(s1): s114006.

[12] Hu H, Qiu B C, He J G, et al. 976 nm wide-stripe semiconductor laser with high-performance [J]. Chinese Journal of Lasers, 2018, 45(8): 0801006.
胡海, 仇伯仓, 何晋国, 等. 高性能 976 nm 宽条半导体激光芯片[J]. 中国激光, 2018, 45(8):

0801006.
[13] Sharfin W F, Seppala J, Mooradian A, et al. High-power, diffraction-limited, narrow-band, external-cavity diode laser[J]. Applied Physics Letters, 1989, 54(18): 1731-1733.
[14] Walpole J N, Kintzer E S, Chinn S R, et al. High-power strained-layer InGaAs/AlGaAs tapered traveling wave amplifier [J]. Applied Physics Letters, 1992, 61(7): 740-742.
[15] Kintzer E S, Walpole J N, Chinn S R, et al. High-power, strained-layer amplifiers and lasers with tapered gain regions[J]. IEEE Photonics Technology Letters, 1993, 5(6): 605-608.
[16] Mathur A, Fisher M, Ziari M, et al. Very high power 1.48 μm semiconductor lasers[J]. Electronics Letters, 1999, 35(12): 983-985.
[17] Kelemen M T, Weber J, Mikulla M, et al. High-power high-brightness tapered diode lasers and amplifiers[J]. Proceedings of SPIE, 2005, 5723: 198.
[18] Swint R B, Yeoh T S, Elarde V C, et al. Curved waveguides for spatial mode filters in semiconductor lasers [J]. IEEE Photonics Technology Letters, 2004, 16(1): 12-14.
[19] Crump P, Leisher P, Matson T, et al. Control of optical mode distribution through etched microstructures for improved broad area laser performance[J]. Applied Physics Letters, 2008, 92(13): 131113.
[20] Fan J A, Belkin M A, Capasso F, et al. Wide-ridge metal-metal terahertz quantum cascade lasers with high-order lateral mode suppression [J]. Applied Physics Letters, 2008, 92(3): 031106.

1064 nm Wide-Ridge Waveguide Semiconductor Laser with Lateral Microstructure

Qi Jun, Zou Yonggang*, Fan Jie**, Yang Jingjing, Liu Ying, Ma Xiaohui

State Key Laboratory of High Power Semiconductor Laser of Changchun University of Science and Technology, Changchun, Jilin 130022, *China*

Abstract

Objective Semiconductor lasers have the advantages of high efficiency, easy integration, high reliability, and easy tuning; hence, they are used in various applications such as fiber coupling, seed laser sources, medical equipment, and communication systems. To increase the output power of semiconductor lasers, a wide-ridge waveguide structure is usually employed; however, in such lasers, the lateral mode is poor and the energy distribution is uneven. These observations are mainly reflected in the "multilobe" phenomenon of the near-field spot, thereby limiting the wide applications of semiconductor lasers. To improve the lateral mode performance of semiconductor lasers, researchers have proposed many solutions including an external cavity laser structure, tapered waveguide structure, and curved waveguide structure. These approaches can improve the lateral mode and quality of the lateral beam. However, they have the disadvantages of low output power, complicated process, and high threshold. In this study, a wide-ridge waveguide semiconductor laser with a lateral microstructure (LMWR-LD) was proposed. Results show that the output power, slope efficiency, and electro-optic conversion efficiency of LMWR-LD were improved, while the mode competition inside the cavity was reduced. Moreover, the lateral microstructure and wide-ridge waveguide structure were formed in the same step of photolithography, which is beneficial to simplify the process and reduce the cost.

Methods Based on the threshold gain theory, the influence of the mode loss on the mode threshold gain was analyzed. As the mode loss increased, the threshold gain of the mode increased. The lateral mode characteristics of wide-ridge waveguide semiconductor laser (WR-LD) were simulated using PIC3D, and the optical field distribution of each order lateral mode was shown (Fig. 2). The fundamental mode optical field was a single spot with a Gaussian distribution, and the energy was mainly concentrated at the center of the optical field. A broken line was observed in the middle of the first-order lateral mode optical field, which was divided into two spots. Thus, the energy distribution of the laser was uneven. When the order index of the lateral mode increased, the number of broken lines in the corresponding lateral mode optical field increased and the energy distribution became more uneven. Based on the characteristics of the optical field distribution of each order lateral mode in WR-LD, the suppression mechanism

of the lateral microstructure on lateral modes (Fig. 3) was observed using FDTD simulation software. The influence of the microstructure width on the mode loss of each order lateral mode was investigated [Fig. 4(a)]. When the microstructure width was fixed, each order lateral mode exhibited different losses. By analyzing the loss difference between the fundamental and high-order lateral modes [Fig. 4(b)], the optimal lateral microstructure width can be obtained. In this case, the loss of the fundamental mode was small and that of the high-order lateral mode was large. Thus, the lateral mode characteristics of LMWR-LD were improved owing to the introduction of microstructure.

Results and Discussions Experimental results show that owing to the fierce competition among each order lateral mode, the near-field spot showed a "mutilobe" appearance in WR-LD [Fig. 5(a)]. After introducing the lateral microstructure, the near-field spot "mutilobe" phenomenon of the LMWR-LD was clearly eliminated [Fig. 5(b)]. Comparing the near-field optical distribution of these two devices, the intensity at the edge of near-field optical distribution for LMWR-LD was observed to decrease significantly [Fig. 5(c)]. This proves that the lateral microstructure had a good inhibition effect on the high-order lateral mode. Because the "multilobe" phenomenon of the near-field optical distribution of LMWR-LD was eliminated, the far-field optical distribution presented a "single-lobe" phenomenon and the full width at half-maximum divergence angle of LMWR-LD decreased from 2.07° to 2.05° (Fig. 6). At 0.5 A input current, the LMWR-LD achieved an output power of 130 mW, showing an improvement of 58.5% compared with WR-LD [Fig. 7(a)]. Moreover, the slope efficiency and electro-optic conversion efficiency of LMWR-LD were 0.27 W/A and 14.5%, respectively, which are 80% and 55.9% higher than those of WR-LD [Fig. 7(b)]. The improvement in slope efficiency and electro-optic conversion efficiency was mainly attributed to the introduction of lateral microstructure. Because the high-order lateral mode was suppressed in the LMWR-LD cavity, the mode competition in the cavity decreased to a certain extent and the optical field distribution of the output laser became more uniform. Therefore, the matching degree of the optical field and injection current was improved.

Conclusions A LMWR-LD structure was proposed in this study. The diffraction loss of the high-order lateral mode was increased by introducing microstructures on both sides of the wide ridge, leading to the suppression of high-order lateral modes. Moreover, the "multilobe" phenomenon in the output laser of LMWR-LD was eliminated. After the fabrication and packaging of LMWR-LD, the test and analysis were conducted. Experimental results show that compared with WR-LD at 0.5 A, the output power of LMWR-LD increased from 82 mW to 130 mW, slope efficiency increased from 0.15 W/A to 0.27 W/A, and the electro-optic conversion efficiency increased from 9.3% to 14.5%. Additionally, the lateral microstructure of LMWR-LD was simultaneously formed with the wide-ridge waveguide structure in ultraviolet lithography. Further, LMWR-LD offers the advantages of simple process and low cost. Based on this research, by optimizing the structure of the device, high-power semiconductor laser devices with good lateral mode characteristics can be achieved.

Key words lasers; semiconductor laser; lateral microstructure; lateral mode; threshold gain; near-field spot

OCIS codes 140.2020;140.5960; 140.3070